Article
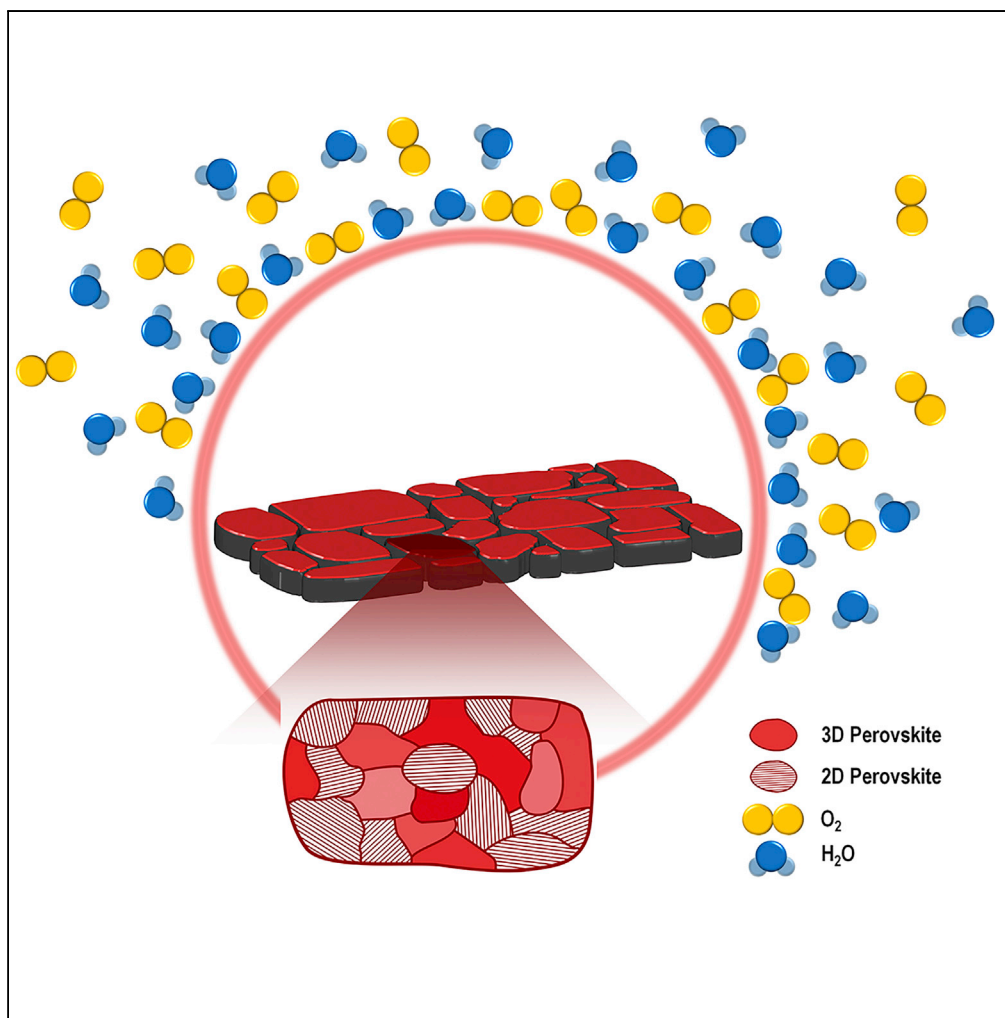
Stable Sn/Pb-Based Perovskite Solar Cells with a Coherent 2D/3D Interface

Ziming Chen,
Meiyue Liu,
Zhenchao Li,
Tingting Shi,
Yongchao Yang,
Hin-Lap Yip, Yong
Cao

msangusyip@scut.edu.cn

HIGHLIGHTS

The 2D perovskite lattice is seamlessly connected to the 3D perovskite lattice

Polymorphs of 2D perovskite were directly observed in a single perovskite film

The best device is among the most stable Sn-based perovskite solar cells to date

Article

Stable Sn/Pb-Based Perovskite Solar Cells with a Coherent 2D/3D Interface

Ziming Chen,[1] Meiyue Liu,[1] Zhenchao Li,[1] Tingting Shi,[1] Yongchao Yang,[1] Hin-Lap Yip,[1,2,3,*] and Yong Cao[1]

SUMMARY

Low-band-gap metal halide perovskite semiconductor based on mixed Sn/Pb is a key component to realize high-efficiency tandem perovskite solar cells. However, the mixed perovskites are unstable in air due to the oxidation of Sn^{2+}. To overcome the stability problem, we introduced N-(3-aminopropyl)-2-pyrrolidinone into the $CH_3NH_3Sn_{0.5}Pb_{0.5}I_xCl_{3-x}$ thin film. The carbonyl group on the molecule interacts with Sn^{2+}/Pb^{2+} by Lewis acid coordination, forming vertically oriented 2D layered perovskite. The 2D phase is seamlessly connected to the bulk perovskite crystal, with a lattice coherently extending across the two phases. Based on this 2D/3D hybrid structure, we assembled low-band-gap Sn-based perovskite solar cells with power conversion efficiency greater than 12%. The best device was among the most stable Sn-based organic-inorganic hybrid perovskite solar cells to date, keeping 90% of its initial performance at ambient condition without encapsulation, and more than 70% under continuous illumination in an N_2-filled glovebox for over 1 month.

INTRODUCTION

Organic-inorganic hybrid perovskite shows excellent optoelectronic properties with high absorption coefficient, high charge carrier mobility, long carrier diffusion lengths, and tunable band gaps, making it a promising light-harvesting layer for next-generation photovoltaic cells (Eperon et al., 2014; Snaith, 2013; Xing et al., 2013; Stranks et al., 2013). After rapid development over the past decade, the pace of perovskite solar cell (PVSC) advancement in terms of power conversion efficiency (PCE) slowed down in the past 2 years, but still reached over 23%, which is on par with the best $CuIn_xGa_{1-x}Se_2$ (CIGS) and CdTe solar cells but lower than that of crystalline Si solar cells (Research Cell Efficiency Records; Accessed November, 2018). One promising strategy to further improve the PCE of PVSCs is to fabricate a tandem solar cell, which is composed of sub-cells with different band gaps to selectively harvest different portions of the solar spectrum to reduce the overall thermalization energy loss during the photocurrent generation process. Several different types of tandem cells were proposed including the perovskite/Si-, perovskite/CIGS-, and perovskite/perovskite-based double-junction cells (Werner et al., 2018; Shen et al., 2018; Eperon et al., 2016; Yu et al., 2016; Meillaud et al., 2006). The first two can be realized by incorporating a large-band-gap (∼1.7–1.9 eV) perovskite cell to harvest the visible light, and the all-perovskite tandem cell requires an additional low-band-gap (∼0.9–1.2 eV) perovskite cell to harvest the near-infrared (NIR) light. The latter one was proved to be feasible because low-band-gap perovskites can be achieved by partially replacing Pb^{2+} with Sn^{2+} in the perovskite lattice and the smallest band gap is achieved when half of the Pb^{2+} is replaced by Sn^{2+} (Ogomi et al., 2014). However, low-band-gap perovskites typically show very poor stability as the bivalent Sn^{2+} in the perovskite is easily oxidized to Sn^{4+} in ambient condition, which destroys the crystal lattice and quickly degrades the device performance (Stoumpos et al., 2013; Wang et al., 2016a). Therefore, although high PCEs of 17%–18% have been demonstrated in low-band-gap PVSCs, the development of stable mixed Sn/Pb-based PVSCs is critically important to realize stable perovskite tandem cells as well as other optoelectronic applications, such as NIR photodetectors and light-emitting diodes (Zhao et al., 2017a; Xu et al., 2018; Zhu et al., 2018; Hong et al., 2016).

Several studies have demonstrated that organic-inorganic two-dimensional (2D) layered perovskites are more stable than three-dimensional (3D) perovskites in terms of ambient stability as the organic layer can serve as a physical barrier to prevent moisture from penetrating into the perovskite film to destroy the perovskite crystal structure (Wang et al., 2018a; Jiang et al., 2018). Therefore, 2D perovskites can improve the stability of perovskite optoelectronic devices, regardless of solar cells or light-emitting diodes (Chen et al., 2017a, 2017b; Yuan et al., 2016; Tsai et al., 2016; Liao et al., 2017). However, unlike 2D perovskite light-emitting diodes, the performance of 2D PVSCs are much more sensitive to the orientation of the

[1]State Key Laboratory of Luminescent Materials and Devices, Institute of Polymer Optoelectronic Materials and Devices, School of Materials Science and Engineering, South China University of Technology, 381 Wushan Road, Guangzhou 510640, P. R. China

[2]Innovation Center for Printed Photovoltaics, South China Institute of Collaborative Innovation, Dongguan 523808, P. R. China

[3]Lead Contact

*Correspondence: msangusyip@scut.edu.cn

2D perovskite planes. In a typical PVSC, laterally oriented 2D layered perovskite is unfavorable as the insulating organic layer could block the charge transport in the vertical direction and reduces the photocurrent. Conversely, in vertically oriented 2D perovskite, charge transportation is not impeded by the insulating organic layer, therefore leading to solar cells with much better PCEs when compared with those having laterally oriented 2D perovskites. Therefore, forming a vertically oriented 2D perovskite is a possible method to achieve stable low-band-gap mixed Sn/Pb-based PVSCs without sacrificing device performance. In recent years, with the introduction of butylammonium (BA) or phenylethylammonium (PEA) in perovskite thin films, it is possible to obtain the desired vertically oriented medium-band-gap 2D perovskites of $(BA)_2(MA)_{n-1}Pb_nI_{3n+1}$, $(PEA)_2(FA)_{n-1}Sn_nI_{3n+1}$, and $(BA)_2Cs_{3x}(MA)_{3-3x}Pb_4I_{13}$ (Tsai et al., 2016; Liao et al., 2017; Chen et al., 2017b, 2018; Zhang et al., 2017a).

As the smallest band gap mixed Sn/Pb perovskite is composed of stoichiometrically identical Sn^{2+} and Pb^{2+}, we therefore attempt to incorporate the most commonly used PEA and BA small molecules into the $CH_3NH_3Sn_{0.5}Pb_{0.5}I_xCl_{3-x}$ perovskite, aiming to create 2D layered perovskites with improved performance (Tsai et al., 2016; Liao et al., 2017). However, unlike the cases in FASnI$_3$- and MAPbI$_3$-based 2D perovskite systems, according to Tables S1 and S2, the incorporation of PEA or BA has a negative effect on the device performance. Therefore, we try to identify a better molecular layer that can possibly form stronger interactions with Sn^{2+} and Pb^{2+} in $CH_3NH_3Sn_{0.5}Pb_{0.5}I_xCl_{3-x}$ to evaluate their effect on the nanostructural control of the perovskite films as well as their corresponding device performance. As we know that solvents containing C=O group such as γ-butyrolactone and N,N-dimethylformamide can interact strongly with the perovskite because the two electron lone pairs on the oxygen atom can make them a Lewis base and coordinate with bivalent metal (Sn^{2+}/Pb^{2+}), which acts as a Lewis acid, they are therefore good solvents for the perovskite precursor solution (Cao et al., 2016, 2017). Moreover, Zhang and co-workers reported that the C=O group in polyvinylpyrrolidone (PVP) could strongly interact with Pb^{2+} ions because of the same reason and that such interaction provided a powerful means to modulate the nucleation and growth of $CH_3NH_3PbI_{3-x}Cl_x$ perovskite (Zhang et al., 2017b). Based on such rationale, we believe that molecules containing C=O group could be a better choice for the formation of vertically oriented 2D low-band-gap perovskite film. Inspired by the chemical structure of PVP, we therefore selected N-(3-aminopropyl)-2-pyrrolidinone (NAP), whose molecular structure is shown in Figure 1A, as the organic molecular layer in our study.

By the incorporation of NAP into the $CH_3NH_3Sn_{0.5}Pb_{0.5}I_xCl_{3-x}$ perovskite, here we demonstrate an interesting 2D/3D hybrid perovskite nanostructure in which a periodic vertically oriented 2D perovskite is seamlessly connected to a 3D perovskite phase, forming a coherent 2D/3D interface. To the best of our knowledge, this is the first report of such a hybrid 2D/3D perovskite structure. Furthermore, we successfully fabricate low-band-gap PVSCs with a PCE of greater than 12% based on the 2D/3D hybrid perovskite structure. More encouragingly, the devices show excellent stability, making them one of the most stable Sn-based PVSCs reported to date.

RESULTS AND DISCUSSION

Morphology and Film Structure

The pristine perovskite film was prepared by spin-coating the precursor solution containing methylammonium iodide (MAI), PbI$_2$, and SnCl$_2$ on poly(3,4-ethylenedioxythiophene)-poly(styrenesulfonate) (PEDOT:PSS) followed by a vacuum annealing process to promote the perovskite crystal formation. Such method facilitates a one-step conversion of the precursor film into perovskite film with negligible amount of Cl in the resultant film (details can be seen in the Methods section) (Liu et al., 2018). The 2D perovskite films were prepared by adding different molar ratios of NAP into the precursor solution, and the same annealing process was applied. Based on the scanning electron microscopic images (top view) in Figure 1B, the pristine film presented a rough surface with some pinholes. After adding 9 and 18 mM NAP to the perovskite films, we obtained smoother films with fewer pinholes. Moreover, when we further increased the NAP concentration to over 36 mM, crystals with more regular shape were formed in the films. As revealed by both the top view and cross-sectional scanning electron microscopic images, square-shaped plate-like crystals with size greater than 1 μm were obtained when the NAP concentration was increased to 144 mM. However, in such sample the crystal grains became more isolated with lower film coverage. Such evolution of perovskite film morphology from irregular to regular crystals suggested that NAP may not only change the morphology of the
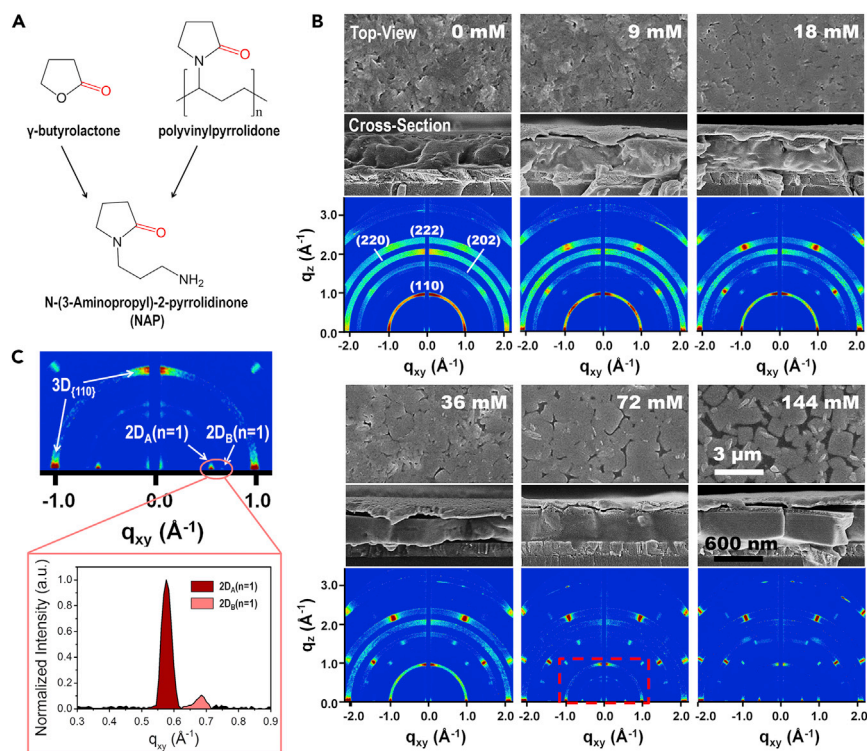
Figure 1. Morphologies and Crystal Orientations of CH$_3$NH$_3$Sn$_{0.5}$Pb$_{0.5}$I$_x$Cl$_{3-x}$ Films with Different Concentrations of NAP

(A) The choice of NAP molecule is inspired by the chemical structures of γ-butyrolactone and polyvinylpyrrolidone, which can strongly interact with perovskite due to the C=O group in the pyrrolidinone unit.

(B) Scanning electron microscopic images (top view/cross-sectional view) and GIWAXS measurements of CH$_3$NH$_3$Sn$_{0.5}$Pb$_{0.5}$I$_x$Cl$_{3-x}$ thin films with different concentrations of NAP.

(C) Magnified image of the marked area in B; besides the 3D$_{\{110\}}$ signals, there are two diffraction dots in the small q_{xy}-value region, which are assigned as the 2D$_A$(n = 1) and 2D$_B$(n = 1) structures of (NAP)$_2$Sn$_{0.5}$Pb$_{0.5}$I$_4$ perovskite, and their normalized signals along the q_{xy} axis are also shown, illustrating that 2D perovskite started to form after adding 72 mM NAP. See the main text for a detailed discussion.

perovskite films but also participate in forming new crystal phases, such as the 2D layered structure as expected.

To further investigate the crystal quality, orientation, and nanostructures of the resultant perovskite films, we also performed grazing-incidence wide-angle X-ray scattering (GIWAXS) study for the different perovskite films, and the results are also shown in Figure 1B. The diffraction rings presented in the GIWAXS pattern of the pristine film suggested that in the absence of NAP, a polycrystalline perovskite film with random crystal orientations was formed. When increasing the concentration of NAP from 9 to 144 mM, the diffraction rings gradually disappeared and changed to several diffraction dots, which suggested that crystals with preferential orientations were formed. Taking the case of 144 mM NAP as an example, the sharp and distinct diffraction dots revealed the formation of highly oriented perovskite thin film, suggesting that the crystals in the corresponding scanning electron microscopic images were almost in the same crystal orientation. More interestingly, according to the GIWAXS data in the case of 72 mM NAP, several diffraction dots appeared in the small q-value region, which is indicated by a red dashed line in Figure 1B, and the corresponding magnified image is shown in Figure 1C for clarity. Along the out-of-plane direction (the q_{xy} axis), two diffraction dots at (q_{xy} = 0.576 Å^{-1}, q_z = 0) and (q_{xy} = 0.683 Å^{-1}, q_z = 0) were observed. The corresponding lattice distance for these two peaks are 10.9 Å and 9.2 Å, respectively, which we assigned to be the polymorphs of the 2D layered (NAP)$_2$Sn$_{0.5}$Pb$_{0.5}$I$_4$ perovskites both containing layer number (n) equal to 1. The one with longer lattice distance is assigned to be 2D$_A$(n = 1), whereas the shorter one is 2D$_B$(n = 1). These two diffraction dots in the out-of-plane direction provide strong evidence that a periodic vertically oriented 2D perovskite phase is formed in the film. It is worth noting that the films
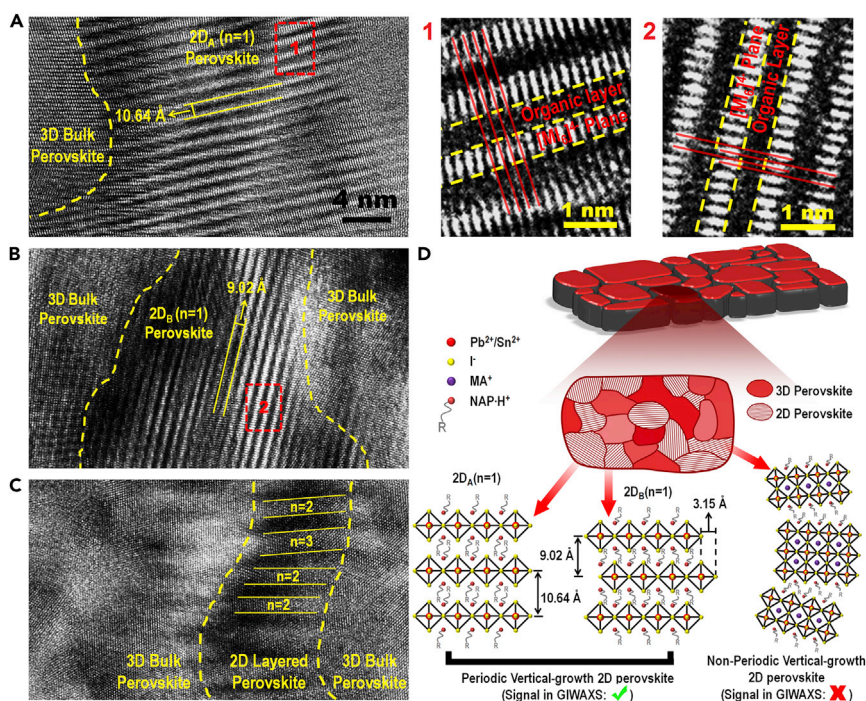
Figure 2. TEM Images of $CH_3NH_3Sn_{0.5}Pb_{0.5}I_xCl_{3-x}$ Thin Film with 72 mM NAP

(A) The $2D_A(n = 1)$ structure and the magnified area 1 (marked with a red dashed line). The red lines in the magnified figure show a head-to-head alignment between adjacent $[MI_6]^{4-}$ planes.

(B) The $2D_B(n = 1)$ structure and the magnified area 2 (marked with a red dashed line). The red lines in the magnified figure show a shift between adjacent $[MI_6]^{4-}$ planes by a distance of half of the lattice.

(C) The non-periodic vertically oriented 2D perovskites contain higher layer numbers.

(D) Schematic diagram of the nanostructure of 2D/3D hybrid perovskite grains.

(A), (B), and (C) have the same magnification, and the scale bar shown in (A) also applies to (B) and (C).

containing high concentrations of NAP are not pure 2D perovskite films, as from the GIWAXS patterns (Figure 1C) we can also observe diffraction dots that are corresponding to the 3D bulk perovskite phase but with better crystal orientation when compared with the randomly oriented ones in the pristine film. Therefore, it is very likely that a 2D/3D hybrid perovskite is formed in the films that contain high concentration of NAP, and it will be very interesting to further study how these different phases are distributed in the film and how they are interacting with each other.

To further evaluate the structural property of the 2D/3D perovskite films, we performed high-resolution transmission electron microscopic (HRTEM) study of the film with 72 mM NAP. As the difference in electron diffraction capabilities can produce a considerable phase contrast between the crystalline $[MI_6]^{4-}$ ($M = Sn^{2+}/Pb^{2+}$) planes and amorphous organic layers, HRTEM offers the chance to directly probe the crystal structures with atomic resolution. To prepare the TEM sample, a poly(methyl methacrylate) (PMMA) precursor solution (100 mg/mL in chlorobenzene) was spin-coated on indium tin oxide (ITO) to form the PMMA layer, followed by the depositions of PEDOT:PSS and perovskite films. The PMMA served as a sacrificing layer and was removed by soaking in chlorobenzene, which is a non-solvent to PEDOT:PSS and perovskite, leaving a floating film of PEDOT:PSS/perovskite that was then picked up by a TEM grid for the study. In such case, we made sure the TEM probing was done from the top of the film, which is important to reveal the vertical orientation of the 2D perovskite phase. The TEM study was performed on multiple areas of the film, and few representation images were used to illustrate our findings. In Figure 2A, an obvious vertically aligned periodic 2D perovskite phase with a repeating distance of 10.64 Å was observed, which correlated very well with the diffraction dot of $2D_A(n = 1)$ perovskite in the GIWAXS result. Most interestingly, the $2D_A(n = 1)$ perovskite phase seamlessly connected to the 3D bulk phase with lattice coherently extended across the two phases (as shown in the magnified TEM image in Figure S1A), forming a very unique 2D/3D perovskite microstructure. Figure 2B shows another vertically oriented 2D perovskite with

a repeating lattice distance of 9.02 Å, which correlated with the diffraction dot of 2D$_B$(n = 1) perovskite in the GIWAXS result. Similar to the case of 2D$_A$(n = 1), the 2D$_B$(n = 1) phase also connected coherently to the 3D bulk perovskite phase as shown in Figure S1B. To the best of our knowledge, this is the first time that polymorphs of 2D metal halide perovskite were directly observed in a single perovskite film. By further analyzing the TEM result, we attribute that the origin of the formation of polymorphs is the difference in arrangement of the adjacent [MI$_6$]$^{4-}$ planes in the 2D$_A$(n = 1) and 2D$_B$(n = 1) structures. In the 2D$_A$(n = 1) structure, according to the magnified image of area 1 in of Figure 2A, all the lattices in the adjacent [MI$_6$]$^{4-}$ planes perfectly aligned with each other, suggesting that there was no lattice shift between adjacent [MI$_6$]$^{4-}$ planes, as depicted in the schematic diagram in Figure 2D. In contrast, according to the magnified image of area 2 of Figure 2B, in the 2D$_B$(n = 1) structure there was a half-lattice shift between adjacent [MI$_6$]$^{4-}$ planes (as also illustrated in Figure 2D). This shift in adjacent [MI$_6$]$^{4-}$ planes alignment also led to the difference in the arrangement of the organic layer, which resulted in the difference in lattice distance between the 2D$_A$(n = 1) (10.64 Å) and 2D$_B$(n = 1) (9.02 Å) perovskite phases. In the latter case, better use of space could be achieved between adjacent [MI$_6$]$^{4-}$ planes, resulting in closer stacking of the organic layer and a smaller repeating distance.

In addition to the polymorphs of 2D perovskite with n = 1, the HRTEM study also revealed that 2D perovskite with higher layer numbers also coexisted in the film. Figure 2C shows that the film contained vertically oriented 2D perovskites with mainly n = 2 and n = 3, which are embedded within the 3D bulk perovskite phase. However, the GIWAXS study did not reveal a diffraction signal of these two types of structures in the small q-value region. We attribute this result to the non-periodic alignment of the n = 2 and n = 3 2D planes (as seen in the TEM image) as well as to the relatively small amount of those phases when compared with the n = 1 2D perovskite, which resulted in the absence of Bragg diffraction and hence the absence of GIWAXS signal.

Solar Cell Performance

To evaluate the photovoltaic properties of the 2D/3D hybrid perovskites solar cells with different concentrations of NAP, solar cell devices were fabricated based on the device architecture of ITO/PEDOT:PSS/perovskite/PCBM/Phen-NaDPO/Ag, as shown in Figure 3A. The best performances of the solar cells are summarized in Table 1, and the statistical performances of 30 devices for each case are summarized in Figure S2. Figures 3B and 3D also show the I-V curves and continuous output of the optimized PVSC based on the 2D/3D hybrid perovskite film to which 72 mM NAP was added, which illustrated a highly stable output with no photocurrent hysteresis for forward and reverse bias scans. With the external quantum efficiency (EQE) edge of low-band-gap CH$_3$NH$_3$Sn$_{0.5}$Pb$_{0.5}$I$_x$Cl$_{3-x}$ PVSCs reaching over 1,000 nm, as shown in Figure 3F, all devices achieved a relatively high short-circuit current density (J_{sc}), suggesting that the formation of periodic vertically oriented 2D perovskite did not impede photocurrent extraction. In addition, the integrated J_{sc} of 0, 9, 18, 36, 72, and 144 mM NAP cases were 23.12, 26.24, 26.06, 25.71, 25.89, and 26.02 mA/cm^2, respectively, which were in the deviation of less than 3.5% compared with the J_{sc} measured under illumination of the solar simulator as shown in Table 1. The obvious shift of EQE spectra after the formation of 2D perovskites was attributed to the enhanced excitonic absorption of 2D perovskite at around 600 nm, as shown in Figure S3. Transient photocurrent measurement (TPC) was also employed to evaluate the charge extraction properties. According to Figure S4A, a longer charge extraction time was observed in pristine PVSC compared with the devices with NAP, illustrating a more efficient charge extraction in NAP-modified devices. In addition, all the NAP-modified devices showed similar charge extraction properties, which also correlated well with the EQE and J_{sc} measurements.

Compared with the pristine device, the addition of 9 mM NAP to the CH$_3$NH$_3$Sn$_{0.5}$Pb$_{0.5}$I$_x$Cl$_{3-x}$ thin film improved all the device parameters, which led to a PCE improvement from 10.3% to 13.4%. We attributed this performance enhancement to the better film morphology (fewer pinholes and a smoother surface) and the better crystal quality, as shown in Figure 1. Also, transient photovoltage measurement (TPV) was employed to study the charge recombination property in PVSCs. According to Figure S4B, the voltage decay time increased with the NAP concentration, illustrating that a slower charge recombination occurred in the perovskite after the introduction of NAP molecules. We attributed this result to the improved perovskite trap passivation effect provided by the NAP molecules (Chen et al., 2017a). However, when 18, 36, and 72 mM NAP were added to the CH$_3$NH$_3$Sn$_{0.5}$Pb$_{0.5}$I$_x$Cl$_{3-x}$ thin films, the device performances dropped slightly, although the films had a better crystal quality, smoother surface, and lower trap density. Therefore, we attributed these slight drops in performance to the increasing number of pinholes and increasing
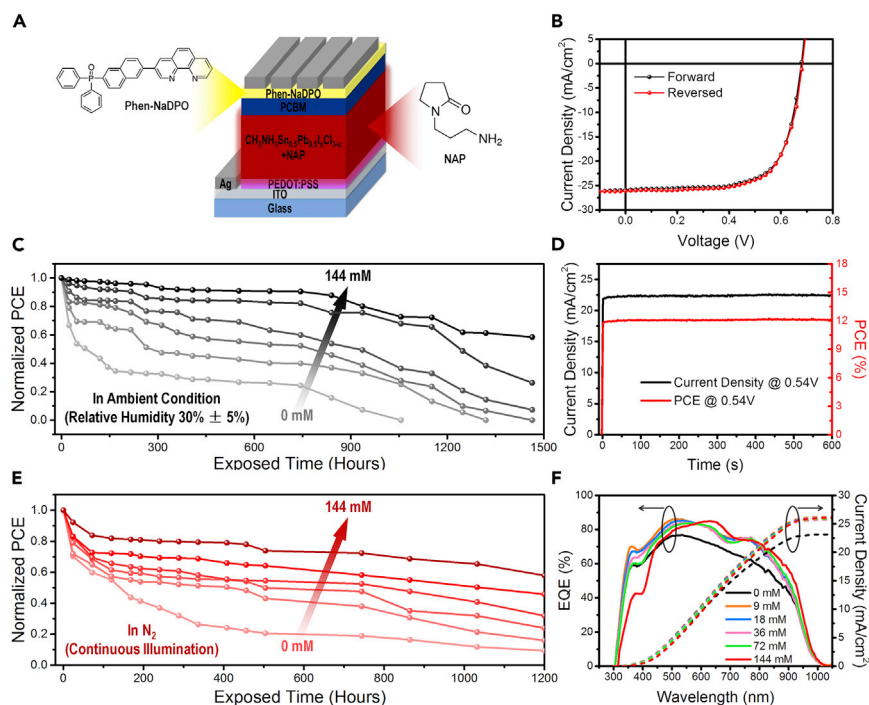
Figure 3. Device Architecture, Performance, and Stability of PVSCs

(A) Solar cell architecture.

(B) I-V curves of PVSC with 72 mM NAP.

(C) Device stability of PVSCs with different concentrations of NAP (average stability of 4 devices). All devices were stored in ambient condition with relative humidity of 30% $\pm$ 5% without any encapsulation.

(D) The time-dependent stabilized power output of the PVSC with 72 mM NAP measured at the maximum power point.

(E) Device stability of PVSCs with different concentrations of NAP under continuous illumination in an N_2-filled glovebox (average stability of 4 devices).

(F) EQEs and the integrated current densities of PVSCs with different concentrations of NAP.

amount of insulated NAP. In the case of perovskite film with 144 mM NAP, despite the film showing excellent crystal quality, relatively low film coverage was obtained. The voids in the perovskite film allowed the contact between the hole and electron transport materials, leading to a further drop in the performance of the solar cell through leakage current. Since the main advantage of the formation of 2D perovskite is improvement of the film stability, we also evaluated the stability of the devices with different concentrations of NAP in addition to their photovoltaic efficiencies. Figure 3C shows that when we increased the NAP concentration in the perovskite films, the devices without any encapsulation showed significant improvement in stability in ambient condition (relative humidity: 30% $\pm$ 5%). The best device was based on the perovskite film to which 144 mM NAP was added, which maintained 90% of its initial performance over 1 month when stored in ambient conditions. On the contrary, devices based on pristine perovskite film showed very poor stability and their performance dropped to less than 50% of the initial value when just stored at ambient conditions for only 3 days. We further evaluated the oxidation state of Sn in perovskite film with and without NAP molecules by X-ray photoelectron spectroscopy. Figure S5 shows that a much slower oxidation rate of Sn^{2+} to Sn^{4+} was found in the 144-mM case compared with the pristine perovskite film, which correlated well with the stability results. Moreover, to mimic the actual working conditions of PVSCs with proper encapsulation, in which water and oxygen content in the device are minimized, we also measured the stability of PVSCs under continuous illumination in an N_2-filled glovebox (H_2O and O_2 < 1 ppm). We also found that the stability of the devices improved significantly as the concentration of NAP in the PVSCs increased, and the best device retained more than 70% of its initial performance after continuous illumination over 1 month, as shown in Figure 3E. It is worth to note that to the best of our knowledge, according to Table S4, our results are one of the most stable Sn-based organic-inorganic hybrid PVSCs reported to date and we attribute the enhanced stability to the formation of 2D/3D perovskite, better crystal quality, and the surface passivation effect provided by the hydrophobic NAP molecules. The last reason is probably

NAP Concentration (mM)	V_{oc} (V)	J_{sc} (mA/cm^2)	FF (%)	PCE (%)
0	0.66	23.3	67.1	10.3
9	0.71	27.1	69.5	13.4
18	0.69	26.7	66.9	12.3
36	0.68	26.3	68.5	12.3
72	0.68	26.1	68.6	12.2
144	0.64	26.5	64.8	10.9

Table 1. Performance of CH$_3$NH$_3$Sn$_{0.5}$Pb$_{0.5}$I$_x$Cl$_{3-x}$ Solar Cells with Different Concentrations of NAP

the most critical one as it had also been reported that in other 2D perovskite films hydrophobic organic layers such as BA and PEA could improve the stability of the perovskite film by providing a physical barrier effect to prevent moisture and oxygen to diffuse into the grain boundary of the perovskite film (Tsai et al., 2016; Liao et al., 2017; Wang et al., 2016b). However, as we have shown in the supporting information, not every organic layer could work well with the Sn/Pb-based perovskite system and only the specially designed NAP provides positive effect both on the device performance and stability, so it will be important to further correlate the molecular design of the organic layer and its chemical interaction with the perovskite to provide better guideline for choosing appropriate molecules to generate the desired hybrid perovskite nanostructures.

Interaction between NAP and Perovskite

The formation of periodic vertically oriented 2D perovskite is strongly related to the interactions between the NAP molecule and the perovskite. In our case, because the two electron lone pairs on the oxygen atom of the C=O group can make the NAP molecule to act as a Lewis base and then coordinate with the bivalent metal (Sn^{2+}/Pb^{2+}), which acts as a Lewis acid, and such coordination could also affect the structural formation of the perovskite (Zhang et al., 2016; Ahn et al., 2015; Wu et al., 2017). To confirm such interaction, we carried out Fourier transform infrared spectroscopy (FTIR) to study the corresponding bonding interaction. According to Figure S6, the featured infrared (IR) absorption of the C=O group in pure NAP was located at wave number of 1,673 cm^{-1} and no signal from the C=O group could be detected in the pristine perovskite film. However, compared with the pristine perovskite, two extra peaks, A and B, appeared in the perovskite film with the NAP molecules. The appearance of a relatively weak peak A (1,673 cm^{-1}) indicated the presence of free C=O groups in the film, whereas the appearance of B (1,625 cm^{-1}) with reduced wave number indicated that the electron density in the C=O group was dragged away from the carbon site by another electron-withdrawing group (which are the bivalent metal Sn^{2+} or Pb^{2+} in our case), which enhanced the IR absorbance of the C=O group, forming a strong peak B with a downshift in the wave number in the FTIR. This result suggests that strong interactions exist between the C=O group and bivalent metals in the film.

To further confirm that the presence of C=O group is critical for the formation of periodic vertically oriented 2D perovskite, we performed a control experiment by adding a reference molecule, 1-(3-aminopropyl)pyrrolidine (chemical structure is shown in Figure S7B), which is structurally similar to NAP but without the C=O group, into the precursor solution. GIWAXS study was also carried out on the perovskite films with different concentrations of 1-(3-aminopropyl)pyrrolidine. As shown in Figure S7A, no diffraction signal appeared in the (q_{xy}<1, q_z = 0) region with different additive concentrations, which suggested that no periodic vertically oriented 2D perovskite was formed after adding 1-(3-aminopropyl)pyrrolidine. Moreover, as the amount of 1-(3-aminopropyl) pyrrolidine in the perovskite thin film increased, the crystal quality of the perovskite gradually decreased. We also fabricated PVSCs with different concentrations of 1-(3-aminopropyl) pyrrolidine based on the device architecture discussed above, and the device performance is summarized in Table S3. The device performance dropped significantly as the amount of 1-(3-aminopropyl)pyrrolidine increased. The dramatic decreases in the J_{sc} also indirectly reflected the unsuccessful formation of the vertically oriented 2D perovskite. According to Figure S8, the poor morphology and rough surface also accounted for the inferior performances of these PVSCs. Particular in the 144-mM case, the irregular crystal shape also suggested poorer crystal quality of perovskite after the introduction of 1-(3-aminopropyl)

pyrrolidine. Therefore, we can conclude that the interaction between the C=O group in NAP and the bivalent metal (Sn^{2+}/Pb^{2+}) plays a major role in the formation of the periodic vertically oriented 2D perovskite structure in our study.

Impact of the Ratio between Sn^{2+} and Pb^{2+}

As the formation of periodic vertically oriented 2D perovskite is related to the interaction between the C=O group in NAP and Sn^{2+} and/or Pb^{2+}, we expected that the ratio between Sn^{2+} and Pb^{2+} would also affect the formation of the structure. Therefore, we modulated the ratio between Sn^{2+} and Pb^{2+} in $CH_3NH_3Sn_yPb_{1-y}I_xCl_{3-x}$ (y = 0, 0.25, 0.5, 0.75, 1) films with 144 mM NAP and again studied their crystallography using GIWAXS. In Figure S9, the $2D_A$(n = 1) and $2D_B$(n = 1) structures have already formed in $CH_3NH_3PbI_xCl_{3-x}$ perovskite with 144 mM NAP. However, the $2D_A$(n = 1) structure grew laterally, whereas the $2D_B$(n = 1) structure mainly grew laterally along with the other orientations. The GIWAXS pattern suggested that the film is polycrystalline. In the $CH_3NH_3Sn_{0.25}Pb_{0.75}I_xCl_{3-x}$ perovskite film with 144 mM NAP, $2D_A$(n = 1) perovskite structure with both lateral and vertical orientations were observed. The diffraction ring of the $2D_B$(n = 1) structure started to change to distinct dots, suggesting the narrowing of the distribution of crystal orientations, and the overall crystal quality also improved. In the $CH_3NH_3Sn_{0.5}Pb_{0.5}I_xCl_{3-x}$ perovskite with 72 mM NAP, both vertically oriented $2D_A$(n = 1) and $2D_B$(n = 1) structures were present in the film, as shown in Figure 1. However, in the $CH_3NH_3Sn_{0.5}Pb_{0.5}I_xCl_{3-x}$ perovskite with 144 mM NAP, most of the $2D_A$(n = 1) structures grew in the vertical direction, whereas the $2D_B$(n = 1) structures almost disappeared. A highly ordered film with an extremely narrow crystal-orientation distribution was obtained in this case. Interestingly, in the $CH_3NH_3Sn_{0.75}Pb_{0.25}I_xCl_{3-x}$ and $CH_3NH_3SnI_xCl_{3-x}$ perovskites with 144 mM NAP, no periodic 2D perovskite was formed and the crystal quality of the films was reduced, according to the GIWAXS study. Therefore, we can conclude that the formation of periodic vertically oriented 2D perovskite is also strongly related to the ratio between Sn^{2+} and Pb^{2+} in the perovskite films as well as the concentration of NAP.

Conclusion

This is the first report that a periodic vertically oriented 2D organic-inorganic hybrid low-band-gap perovskite could be formed by introducing specially designed molecule into a $CH_3NH_3Sn_{0.5}Pb_{0.5}I_xCl_{3-x}$ precursor solution. The GIWAXS results revealed two types of periodic vertically oriented 2D perovskites in the film, which were assigned as $2D_A$(n = 1) and $2D_B$(n = 1). In the $2D_A$(n = 1) structure, the adjacent $[MI_6]^{4-}$ planes perfectly aligned with each other, whereas a half-lattice shift between adjacent $[MI_6]^{4-}$ planes was observed in the $2D_B$(n = 1) structure. In the HRTEM study, we observed both non-periodic and periodic vertically oriented 2D perovskite structures and both of them seamlessly connected with the 3D bulk phase of the perovskite. The former one is typically formed by the 2D perovskite with higher layer numbers, whereas the latter one is formed when the layer number is equal to 1. Furthermore, we studied the factors that affected the formation of the periodic vertically oriented 2D perovskite structure. The interaction between the C=O group in NAP and Sn^{2+}/Pb^{2+} was found to be important to promote the formation of such structure, and the ratio between Sn^{2+} and Pb^{2+} in the perovskite films and the concentration of NAP also affected its formation.

Eventually, we have successfully fabricated a stable low-band-gap Sn-based PVSC based on the 2D/3D hybrid perovskite structure. Our optimized PVSC achieves a PCE of greater than 12%, which is the best reported result based on a 2D/3D hybrid low-band-gap perovskite. The devices also show improved ambient stability and illuminated stability as the NAP concentration increases, making one of the most stable Sn-based organic-inorganic hybrid PVSCs, which suggests that the formation of 2D/3D perovskite could provide a solution to the degradation of Sn-based perovskite.

METHODS

All methods can be found in the accompanying Transparent Methods supplemental file.

Limitations of Study

In this study, we observed that the introduction of NAP slowed down the oxidation process of Sn^{2+} to Sn^{4+} in perovskite films in ambient condition, which facilitated a better ambient stability of Sn-based PVSCs. However, we could not show a fundamental mechanism or a convincing reason for this observation. More investigation is needed to further reveal the role of NAP in perovskite stability, as which is possible to promote a development of stable Sn-based PVSCs.

REFERENCES

Ahn, N., Son, D.Y., Jang, I.H., Kang, S.M., Choi, M., and Park, N.G. (2015). Highly reproducible perovskite solar cells with average efficiency of 18.3% and best efficiency of 19.7% fabricated via Lewis base adduct of lead(II) iodide. J. Am. Chem. Soc. *137*, 8696–8699.

Cao, X., Li, C., Li, Y., Fang, F., Cui, X., Yao, Y., and Wei, J. (2016). Enhanced performance of perovskite solar cells by modulating the Lewis acid-base reaction. Nanoscale *8*, 19804.

Cao, X.B., Li, C.L., Zhi, L.L., Li, Y.H., Cui, X., Yao, Y.W., Ci, L.J., and Wei, J.Q. (2017). Fabrication of high quality perovskite films by modulating the Pb-O bonds in Lewis acid-base adducts. J. Mater. Chem. A *5*, 8416.

Chen, Z., Zhang, C., Jiang, X.-F., Liu, M., Xia, R., Shi, T., Chen, D., Xue, Q., Zhao, Y.-J., Su, S., et al. (2017a). High-performance color-tunable perovskite light emitting devices through structural modulation from bulk to layered film. Adv. Mater. *29*, 1603157.

Chen, Y., Sun, Y., Peng, J., Zhang, W., Su, X., Zheng, K., Pullerits, T., and Liang, Z. (2017b). Tailoring organic cation of 2D air-stable organometal halide perovskites for highly efficient planar solar cells. Adv. Energy Mater. *7*, 1700162.

Chen, A.Z., Shiu, M., Ma, J.H., Alpert, M.R., Zhang, D., Foley, B.J., Smilgies, D.-M., Lee, S.-H., and Choi, J.-J. (2018). Origin of vertical orientation in two-dimensional metal halide perovskites and its effect on photovoltaic performance. Nat. Commun. *9*, 1336.

Eperon, G.E., Stranks, S.D., Menelaou, C., Johnston, M.B., Herz, L.M., and Snaith, H.J. (2014). Formamidinium lead trihalide: a broadly tunable perovskite for efficient planar heterojunction solar cells. Energy Environ. Sci. *7*, 982–988.

Eperon, G.E., Leijtens, T., Bush, K.A., Prasanna, R., Green, T., Wang, J.T.-W., McMeekin, D.P., Volonakis, G., Milot, R.L., May, R., et al. (2016). Perovskite-perovskite tandem photovoltaics with optimized bandgaps. Science *354*, 861–865.

Hong, W.-L., Huang, Y.-C., Chang, C.-Y., Zhang, Z.-C., Tsai, H.-R., Chang, N.-Y., and Chao, Y.-C. (2016). Efficient low-temperature solution-processed lead-free perovskite infrared light-emitting diodes. Adv. Mater. *28*, 8029–8036.

Jiang, Y., Yuan, J., Ni, Y., Yang, J., Wang, Y., Jiu, T., Yuan, M., and Chen, J. (2018). Reduced-dimensional a-CsPbX$_3$ perovskites for efficient and stable photovoltaics. Joule *2*, 1356–1368.

Liao, Y., Liu, H., Zhou, W., Yang, D., Shang, Y., Shi, Z., Li, B., Jiang, X., Zhang, L., Quan, L.N., et al. (2017). Highly oriented low-dimensional tin halide perovskites with enhanced stability and photovoltaic performance. J. Am. Chem. Soc. *139*, 6693–6699.

Liu, M., Chen, Z., Xue, Q., Cheung, S.H., So, S.-K., Yip, H.-L., and Cao, Y. (2018). High performance low-bandgap perovskite solar cells based on high-quality mixed Sn-Pb perovskite film prepared by vacuum-assisted thermal annealing. J. Mater. Chem. A *6*, 16347–16354.

Meillaud, F., Shah, A., Droz, C., Vallat-Sauvain, E., and Miazza, C. (2006). Efficiency limits for single-junction and tandem solar cells. Sol. Energy Mater. Sol. Cells *90*, 2952–2959.

Ogomi, Y., Morita, A., Tsukamoto, S., Saitho, T., Fujikawa, N., Shen, Q., Toyoda, T., Yoshino, K., Pandey, S.S., Ma, T., et al. (2014). CH$_3$NH$_3$Sn$_x$Pb$_{(1-x)}$I$_3$ perovskite solar cells covering up to 1060 nm. J. Phys. Chem. Lett. *5*, 1004–1011.

Research Cell Efficiency Records. https://www.nrel.gov/pv/assets/pdfs/pv-efficiencies-07-17-2018.pdf Accessed November, 2018.

Shen, H., Duong, T., Peng, J., Jacobs, D., Wu, N., Gong, J., Wu, Y., Karuturi, S.K., Fu, X., Weber, K., et al. (2018). Mechanically-stacked perovskite/CIGS tandem solar cells with efficiency of 23.9% and reduced oxygen sensitivity. Energy Environ. Sci. *11*, 394–406.

Snaith, H.J. (2013). Perovskites: the emergence of a new era for low-cost, high-efficiency solar cells. J. Phys. Chem. Lett. *4*, 3623–3630.

Stoumpos, C.C., Malliakas, C.D., and Kanatzidis, M.G. (2013). Semiconducting tin and lead iodide perovskites with organic cations: phase transitions, high mobilities, and near-infrared photoluminescent properties. Inorg. Chem. *52*, 9019–9038.

Stranks, S.D., Eperon, G.E., Grancini, G., Menelaou, C., Alcocer, M.J.P., Leijtens, T., Herz, L.M., Petrozza, A., and Snaith, H.J. (2013). Electron-hole diffusion lengths exceeding 1 micrometer in an organometal trihalide perovskite absorber. Science *342*, 341–344.

Tsai, H., Nie, W., Blancon, J.C., Stoumpos, C.C., Asadpour, R., Harutyunyan, B., Neukirch, A.J., Verduzco, R., Crochet, J.J., Tretiak, S., et al. (2016). High-efficiency two-dimensional Ruddlesden-Popper perovskite solar cells. Nature 536, 312–316.

Wang, F., Ma, J.L., Xie, F., Li, L., Chen, J., Fan, J., and Zhao, N. (2016a). Organic cation-dependent degradation mechanism of organotin halide perovskites. Adv. Funct. Mater. 26, 3417–3423.

Wang, F., Geng, W., Zhou, Y., Fang, H.-H., Tong, C.-J., Loi, M.A., Liu, L.-M., and Zhao, N. (2016b). Phenylalkylamine passivation of organolead halide perovskites enabling high-efficiency and air-stable photovoltaic cells. Adv. Mater. 28, 9986–9992.

Wang, Y., Zhang, T., Kan, M., Li, Y., Wang, T., and Zhao, Y. (2018a). Efficient a-CsPbI₃ photovoltaics with surface terminated organic cations. Joule 2, https://doi.org/10.1016/j.joule.2018.06.013.

Werner, j., Niesen, B., and Ballif, C. (2018). Perovskite/silicon tandem solar cells: marriage of convenience or true love story? – an overview. Adv. Mater. Interfaces 5, 1700731.

Wu, Z., Raga, S.R., Juarez-Perez, E.J., Yao, X., Jiang, Y., Ono, L.K., Ning, Z., Tian, H., and Qi, Y.B. (2017). Improved efficiency and stability of perovskite solar cells induced by C=O functionalized hydrophobic ammonium based additives. Adv. Mater. 30, 1703670.

Xing, G.-C., Mathews, N., Sun, S.-Y., Lim, S.S., Lam, Y.M., Grätzel, M., Mhaisalkar, S., and Sum, T.C. (2013). Long-range balanced electron and hole-transport lengths in organic-inorganic CH₃NH₃PbI₃. Science 342, 344–347.

Xu, G., Bi, P., Wang, S., Xue, R., Zhang, J., Chen, H., Chen, W., Hao, X., Li, Y., and Li, Y. (2018). Integrating ultrathin bulk-heterojunction organic semiconductor intermediary for high-performance low bandgap perovskite solar cells with low energy loss. Adv. Funct. Mater. 28, 1804427.

Yu, Z., Leilaeioun, M., and Holman, Z. (2016). Selecting tandem partners for silicon solar cells. Nat. Energy 1, 16137.

Yuan, M., Quan, L.N., Comin, R., Walters, G., Sabatini, R., Voznyy, O., Hoogland, S., Zhao, Y., Beauregard, E.M., Kanjanaboos, P., et al. (2016). Perovskite energy funnels for efficient light-emitting diodes. Nat. Nanotechnol. 11, 872–877.

Zhang, Y., Gao, P., Oveisi, E., Lee, Y., Jeangros, Q., Grancini, G., Paek, S., Feng, Y., and Nazeeruddin, M.K. (2016). PbI₂-HMPA complex pretreatment for highly reproducible and efficient CH₃NH₃PbI₃ perovskite solar cells. J. Am. Chem. Soc. 138, 14380–14387.

Zhang, X., Ren, X., Liu, B., Munir, R., Zhu, X., Yang, D., Li, J., Liu, Y., Smilgies, D.-M., Li, R., et al. (2017a). Stable high efficiency two-dimensional perovskite solar cells via cesium doping. Energy Environ. Sci. 10, 2095–2102.

Zhang, Y., Zhuang, X., Zhou, K., Cai, C., Hu, Z., Zhang, J., and Zhu, Y. (2017b). Amorphous polymer with C=O to improve the performance of perovskite solar cells. J. Mater. Chem. C 5, 9037–9043.

Zhao, D., Yu, Y., Wang, C., Liao, W., Shrestha, N., Grice, C.R., Cimaroli, A.J., Guan, L., Ellingson, R.J.E., Zhu, K., et al. (2017a). Low-bandgap mixed tin–lead iodide perovskite absorbers with long carrier lifetimes for all-perovskite tandem solar cells. Nat. Energy 2, 17018.

Zhu, H.L., Liang, Z., Huo, Z., Ng, W.K., Mao, J., Wong, K.S., Yin, W.-J., and Choy, W.C.H. (2018). Low-bandgap methylammonium-rubidium cation Sn-rich perovskites for efficient ultraviolet–visible–near infrared photodetectors. Adv. Funct. Mater. 28, 1706068.
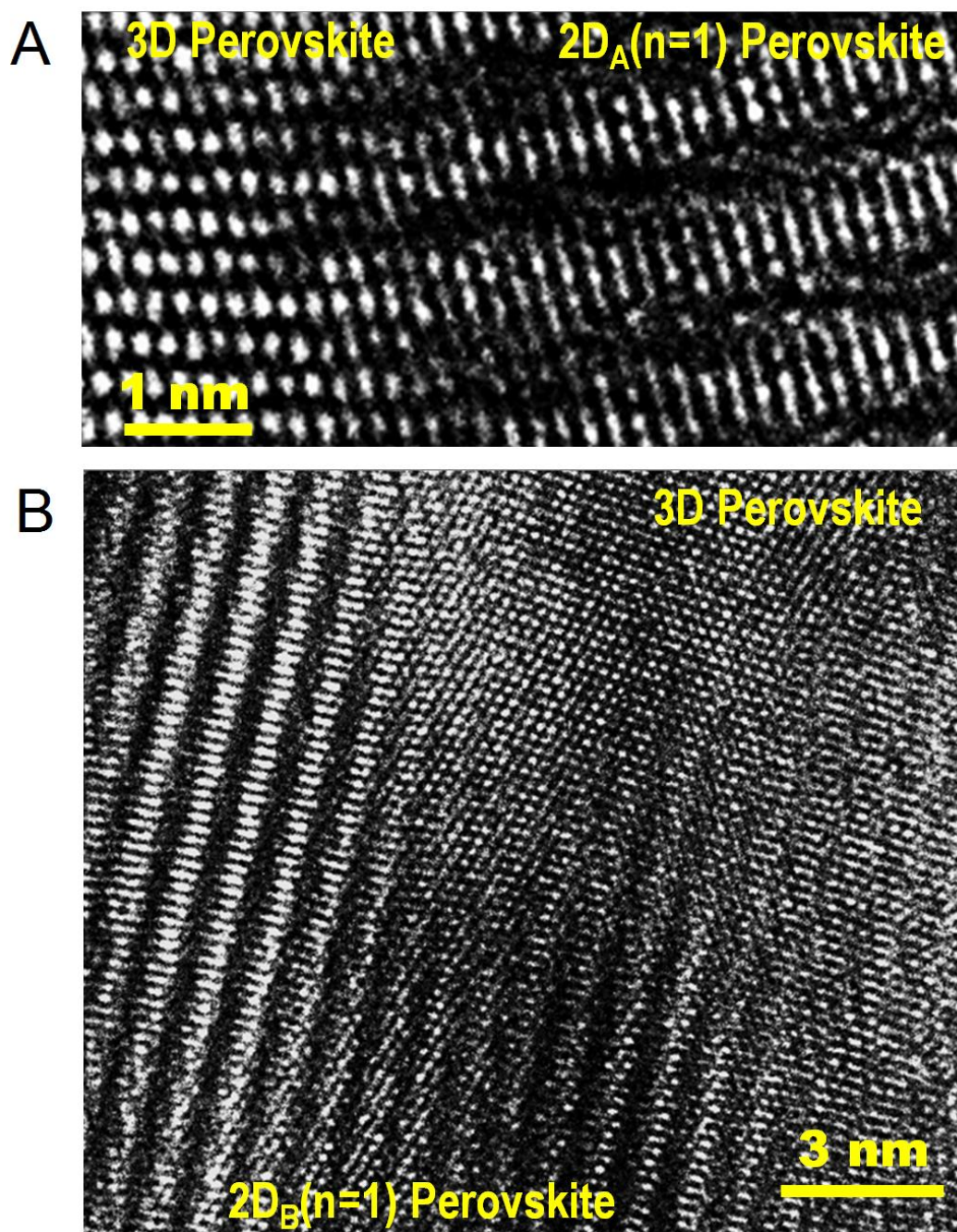
Supplemental Information

# Stable Sn/Pb-Based Perovskite Solar Cells

with a Coherent 2D/3D Interface

Ziming Chen, Meiyue Liu, Zhenchao Li, Tingting Shi, Yongchao Yang, Hin-Lap Yip, and Yong Cao

Supplemental Information

**Figure S1. The detailed configurations of 2D/3D hybrid structure in HRTEM images, related to**

Figure 2. (**A**) $2D_A$(n=1) perovskite seamlessly connects to 3D bulk perovskite. (**B**) $2D_B$(n=1)

perovskite seamlessly connects to 3D bulk perovskite. These results suggest that the growths of 2D and

3D structures are correlated.
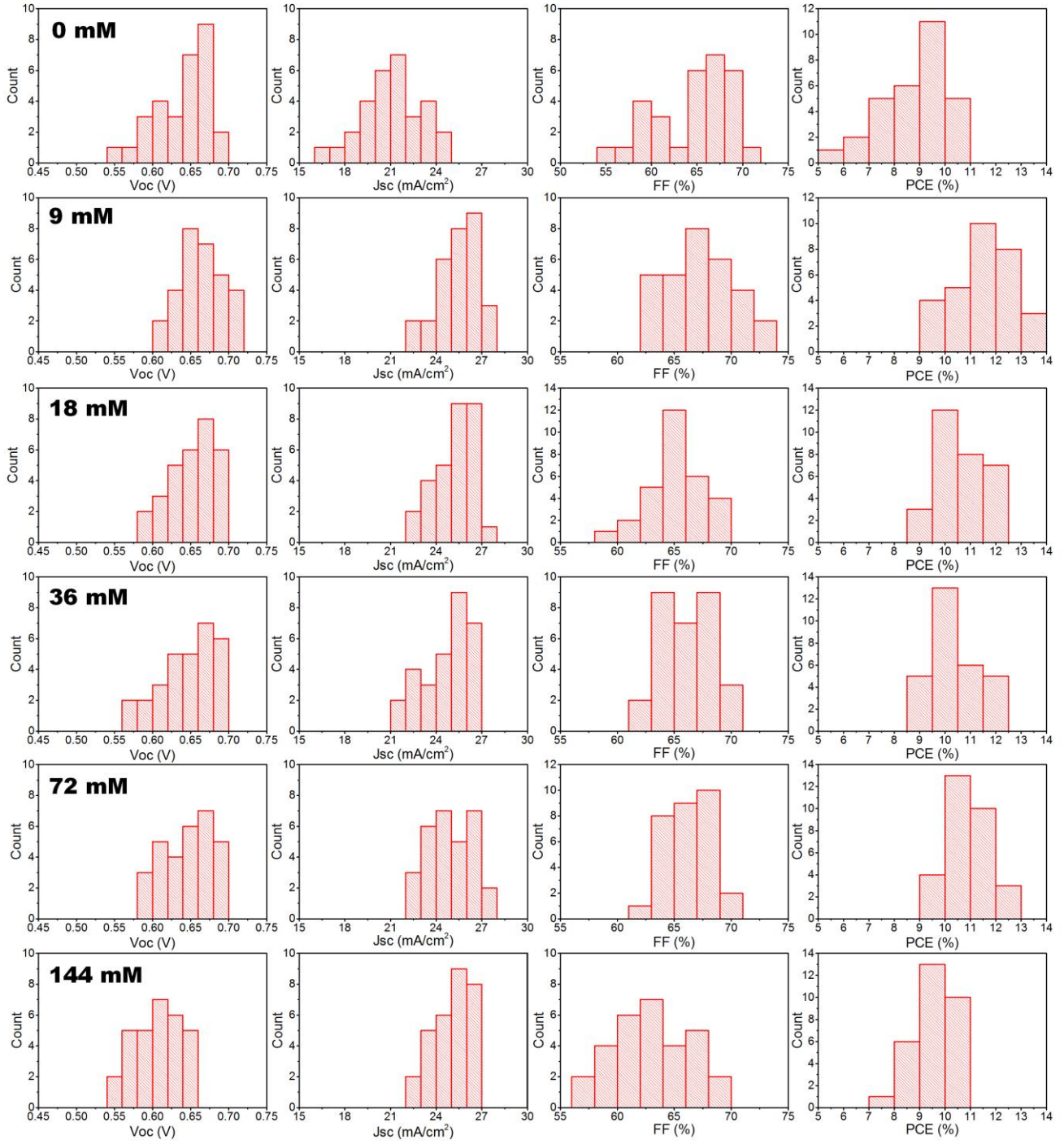
Figure S2. Statistical performances of $CH_3NH_3Sn_{0.5}Pb_{0.5}I_xCl_{3-x}$ perovskite solar cells with different concentrations of NAP, related to Table 1. We collected the data from 30 devices in each case.
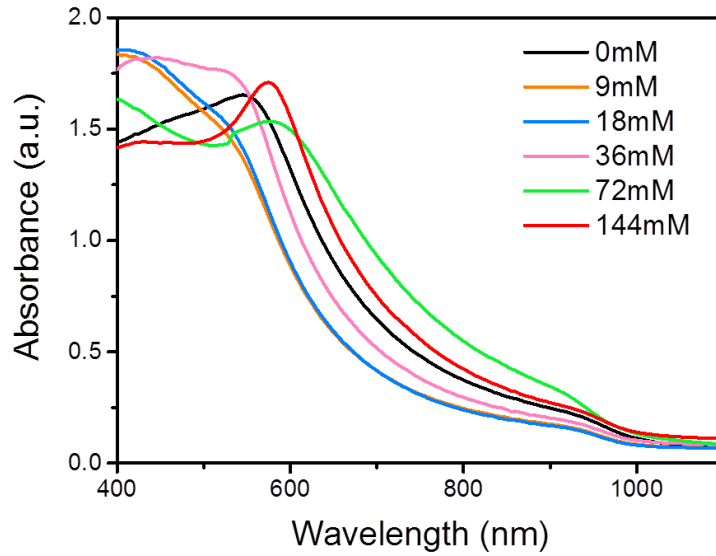
Figure S3. Absorptions of CH₃NH₃Sn₀.₅Pb₀.₅IₓCl₃₋ₓ perovskites with different concentrations of NAP, related to Figure 3. The absorption peak at around 600 nm is the excitonic absorption of 2D perovskite.
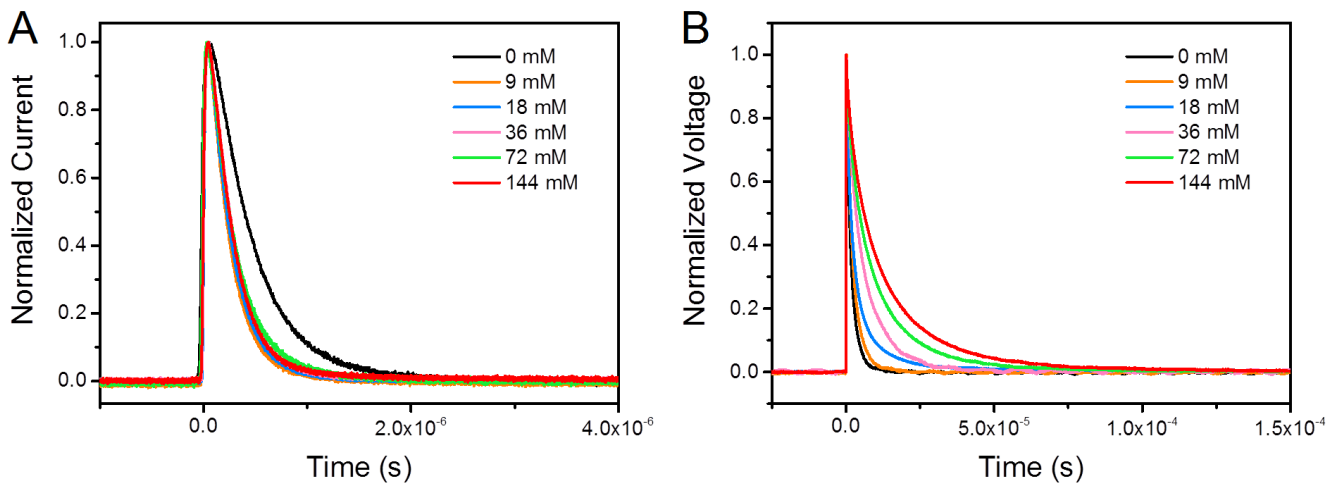

Figure S4. Charge extraction and recombination properties of CH₃NH₃Sn₀.₅Pb₀.₅IₓCl₃₋ₓ perovskite with different concentrations of NAP, related to Figure 3. (A) TPC measurement and **(B)** TPV measurement.
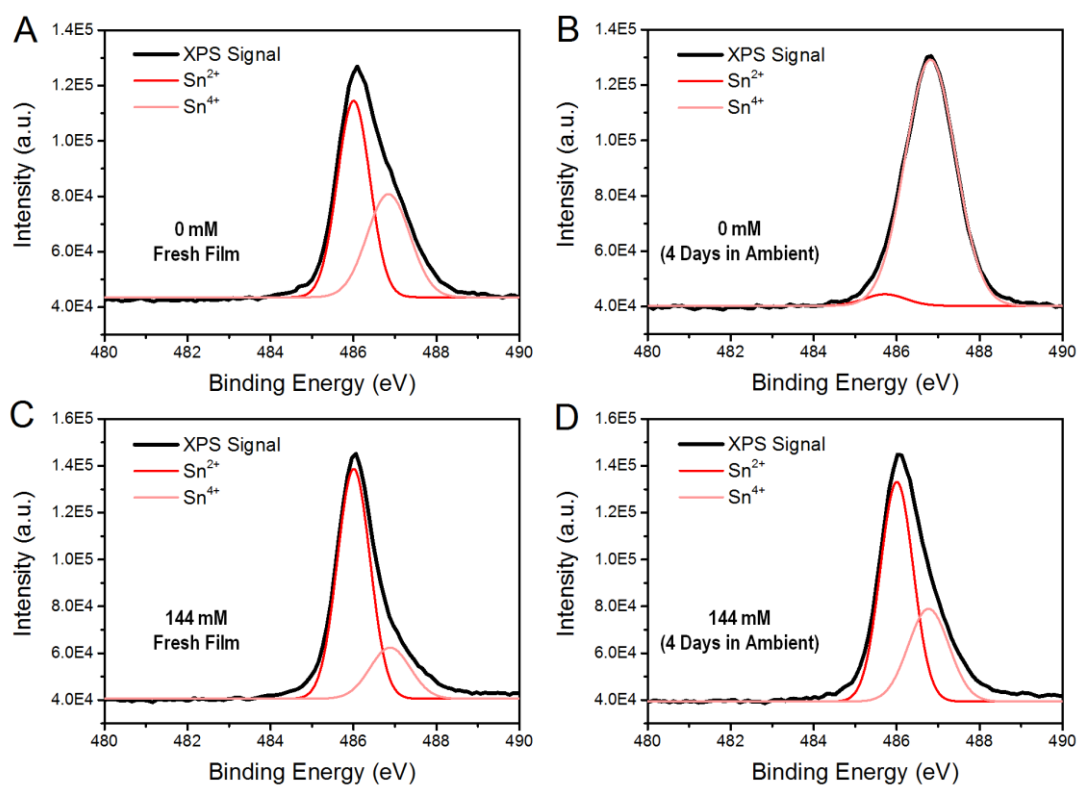
**Figure S5. XPS measurement of Sn3d signal in CH₃NH₃Sn₀.₅Pb₀.₅IₓCl₃₋ₓ film with and without**

144 mM NAP, related to Figure 3. (**A**) Fresh $CH_3NH_3Sn_{0.5}Pb_{0.5}I_xCl_{3-x}$ film. (**B**)

$CH_3NH_3Sn_{0.5}Pb_{0.5}I_xCl_{3-x}$ film after exposure in ambient condition for 4 days. (**C**) Fresh

$CH_3NH_3Sn_{0.5}Pb_{0.5}I_xCl_{3-x}$ film with 144 mM NAP. (**D**) $CH_3NH_3Sn_{0.5}Pb_{0.5}I_xCl_{3-x}$ film with 144 mM NAP

after exposure in ambient condition for 4 days.
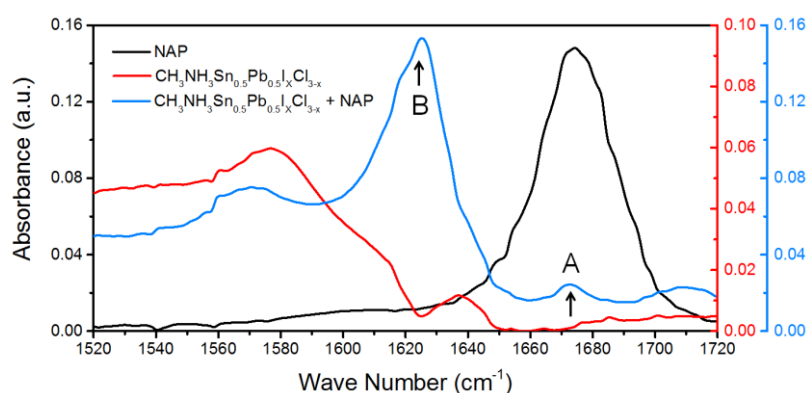
Figure S6. FTIR of CH₃NH₃Sn₀.₅Pb₀.₅IₓCl₃₋ₓ perovskite with and without 72 mM NAP, related to

Figure 1. The extra peaks of A and B in the blue curve indicate the signal of the C=O bond.
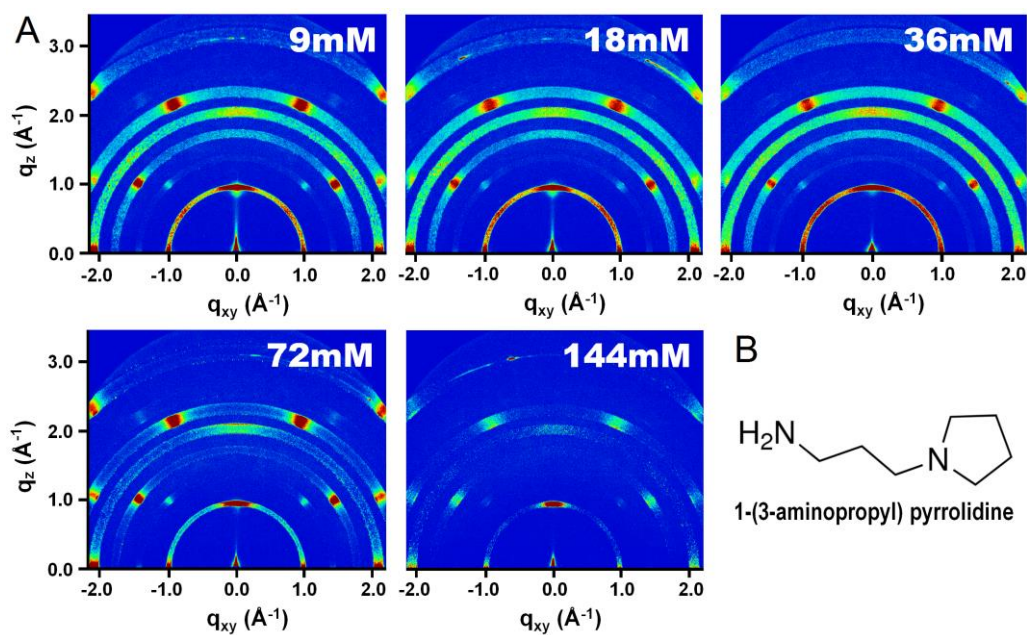
Figure S7. Crystal quality of $CH_3NH_3Sn_{0.5}Pb_{0.5}I_xCl_{3-x}$ thin films with different concentrations of 1-(3-aminopropyl) pyrrolidine, related to Figure 1. (**A**) GIWAXS study of $CH_3NH_3Sn_{0.5}Pb_{0.5}I_xCl_{3-x}$ thin films with different concentrations of 1-(3-aminopropyl) pyrrolidine. (**B**) Molecular structure of 1-(3-aminopropyl) pyrrolidine.
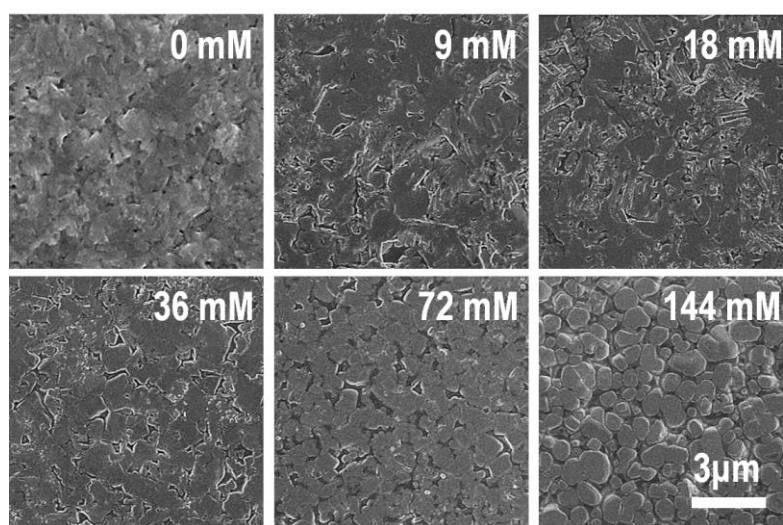
Figure S8. Morphologies of $CH_3NH_3Sn_{0.5}Pb_{0.5}I_xCl_{3-x}$ thin films with different concentrations of 1-(3-aminopropyl) pyrrolidine, related to Figure 1.
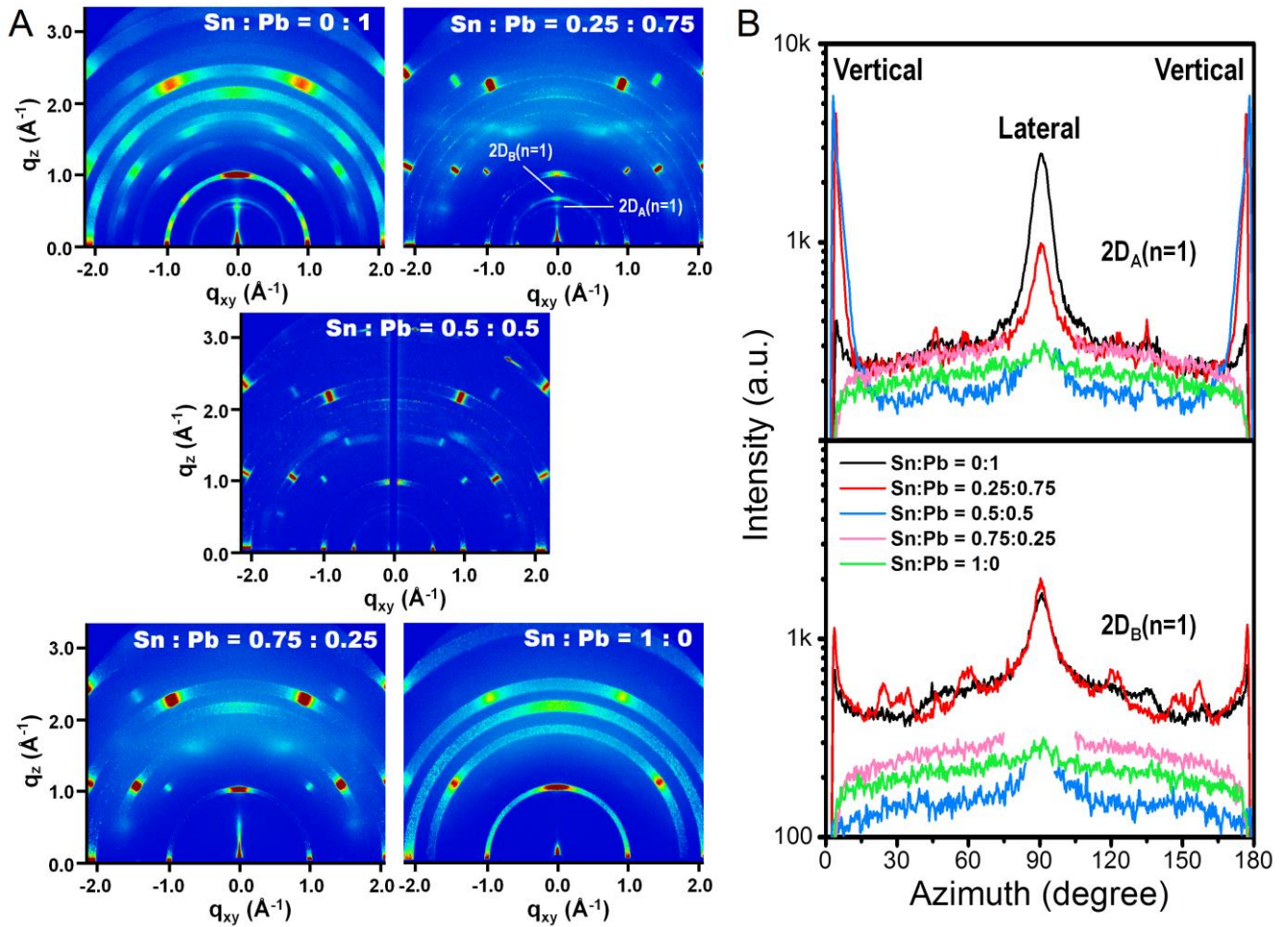
Figure S9. The effect of the ratio of Sn^{2+} to Pb^{2+} on the formation of periodic vertically oriented 2D perovskite, related to Figure 1. (**A**) GIWAXS study of $CH_3NH_3Sn_yPb_{1-y}I_xCl_{3-x}$ (y = 0, 0.25, 0.5, 0.75, 1) thin films with 144 mM NAP. (**B**) Radially integrated intensity plots along the ring at $q = 0.576$ $Å^{-1}$ and $q = 0.683$ $Å^{-1}$, corresponding to $2D_A(n=1)$ and $2D_B(n=1)$ structures, respectively. For fair comparison, the data around $90°$ in $CH_3NH_3Sn_{0.75}Pb_{0.25}I_xCl_{3-x}$ were eliminated because the signal in this region mainly came from the reflected X-ray rather than diffraction. The periodic 2D perovskites only existed in the $CH_3NH_3Sn_yPb_{1-y}I_xCl_{3-x}$ films (y = 0, 0.25, 0.5) and their orientations gradually transferred from the lateral to the vertical direction as the amount of Sn increased.

Table S1. Performances of $CH_3NH_3Sn_{0.5}Pb_{0.5}I_xCl_{3-x}$ solar cells with different concentrations of PEA, related to Table 1. The device architecture was ITO/PEDOT:PSS/perovskite/PCBM/ Phen-NaDPO/Ag.

Concentration	V_{oc} (V)	J_{sc} (mA/cm^2)	FF (%)	PCE (%)
0 mM	0.66	23.3	67.1	10.3
9 mM	0.60	25.1	63.2	9.53
18 mM	0.56	24.7	61.8	8.56
36 mM	0.55	23.3	60.5	7.80
72 mM	0.54	22.3	58.8	7.10
144 mM	0.53	21.6	53.4	6.11

Table S2. Performances of $CH_3NH_3Sn_{0.5}Pb_{0.5}I_xCl_{3-x}$ solar cells with different concentrations of BA, related to Table 1. The device architecture was ITO/PEDOT:PSS/perovskite/PCBM/ Phen-NaDPO/Ag.

Concentration	V_{oc} (V)	J_{sc} (mA/cm^2)	FF (%)	PCE (%)
0 mM	0.66	23.3	67.1	10.3
9 mM	0.58	24.4	66.8	9.44
18 mM	0.52	23.5	66.2	8.09
36 mM	0.51	21.7	63.5	7.04
72 mM	0.50	21.5	60.2	6.50
144 mM	0.47	21.0	57.7	5.68

Table S3. Performances of $CH_3NH_3Sn_{0.5}Pb_{0.5}I_xCl_{3-x}$ solar cells with different concentrations of 1-(3-aminopropyl) pyrrolidine, related to Table 1. The device architecture was ITO/PEDOT:PSS/perovskite/PCBM/ Phen-NaDPO/Ag.

Concentration	V_{oc} (V)	J_{sc} (mA/cm^2)	FF (%)	PCE (%)
0 mM	0.66	23.3	67.1	10.3
9 mM	0.60	16.45	73.4	7.19
18 mM	0.57	15.46	63.8	5.64
36 mM	0.56	11.79	65.9	4.32
72 mM	0.55	5.73	65.7	2.09
144 mM	0.50	2.53	57.3	0.73

Table S4. Summary of lifetimes of Sn-based organic-inorganic hybrid perovskite solar cells, related to Figure 3.

Composition	Aged Conditions (Without Encapsulation)	Lifetime	Ref
$(PEA)_2(FA)_{n-1}Sn_nI_{3n+1}$	Stored in an N_2-filled glovebox	$T_{96}=100$ h	Liao et al., 2017
$FA_{0.75}MA_{0.25}SnI_3$	Stored in an N_2-filled glovebox	$T_{80}=400$ h	Zhao et al., 2017
$(FASnI_3)_{0.6}(MAPbI_3)_{0.4}$	Stored in an N_2-filled glovebox	$T_{80}=600$ h	Xu et al., 2018
$FA_{0.7}MA_{0.3}Sn_{0.3}Pb_{0.7}I_3$	Stored in an N_2-filled glovebox	$T_{80}=720$ h	Wang et al., 2018
$MAPb_{0.5}Sn_{0.5}(I_{0.8}Br_{0.2})_3$	Stored in an N_2-filled glovebox	$T_{92}=720$ h	Yang et al., 2017
$MA_{0.5}FA_{0.5}Pb_{0.75}Sn_{0.25}I_3$	Stored in an N_2-filled glovebox	$T_{94}=720$ h	Yang et al., 2016
$(FAPbI_3)_{0.7}(CsSnI_3)_{0.3}$	Stored in an N_2-filled glovebox	$T_{98.3}=288$ h	Zong et al., 2018
$MA_{0.5}FA_{0.5}Pb_{0.5}Sn_{0.5}I_3$	Stored in an N_2-filled glovebox	$T_{99}=720$ h	Xu et al., 2017
$(NAP)_2(MA)_{n-1}(Sn_{0.5}Pb_{0.5})_nI_{3n+1}$	Under continuous illumination in an N_2-filled glovebox	$T_{70}=720$ h	This work
Composition	**Aged Conditions (Without Encapsulation)**	**Lifetime**	**Ref**
$FASnI_3$	Stored in ambient condition, with illumination	$T_{50}=1$ h	Ke et al., 2017
$MAPb_{0.5}Sn_{0.5}(I_{0.8}Br_{0.2})_3$	Stored in ambient condition, 30–50% RH	$T_{44}=336$ h	Yang et al., 2017
$MAPb_{0.75}Sn_{0.25}I_3$	Stored in ambient condition, 30–40% RH	$T_{80}=96$ h	Yang et al., 2016
$MAPb_{0.75}Sn_{0.25}I_3$	Stored in ambient condition, 30–50% RH	$T_{80}=168$ h	Liu et al., 2017
$MA_{0.5}FA_{0.5}Pb_{0.75}Sn_{0.25}I_3$	Stored in ambient condition, 30–40% RH	$T_{80}=288$ h	Yang et al., 2016
$FASnI_3$	Stored in ambient condition, encapsulated	$T_{85}=720$ h	Liao et al., 2016
$(FAPbI_3)_{0.7}(CsSnI_3)_{0.3}$	Stored in ambient condition, 20% relative humidity (RH)	$T_{90}=288$ h	Zong et al., 2018
$(NAP)_2(MA)_{n-1}(Sn_{0.5}Pb_{0.5})_nI_{3n+1}$	Stored in ambient condition, 30 % ± 5 % RH	$T_{90}=720$ h	This work

Transparent Methods

Perovskite solution preparation

A mixture of 4 mmol of MAI, 1 mmol of PbI_2 and 1 mmol of $SnCl_2$ were dissolved in 1 ml DMF to form a pristine perovskite precursor solution. Subsequently, appropriate NAP (or 1-(3-aminopropyl) pyrrolidine) molecules were added into the pristine precursor solution in the concentration of x mM. The solution was stirred at room temperature for one day.

Perovskite film characterization

The SEM images were obtained in the sample structure of ITO/PEDOT:PSS/perovskite, using a Zeiss EVO 18. GIWAXS measurement was carried out with a sample structure of quartz/PEDOT:PSS/perovskite by Xeuss 2.0 (Xenocs company) with MetalJet-D2 (Excillum) as the X-ray source and Pilatus3R 1M (Dectris) as the detector. FTIR spectra were recorded by a Thermo Scientific Nicolet iS 50 in transmittance model. TEM samples were prepared according to the structure of ITO/PMMA/PEDOT:PSS/perovskite. The PMMA film was dissolved in chlorobenzene, and the PEDOT:PSS/perovskite film could be separated from the substrate, which was suitable for TEM measurement. The TEM samples were measured by JEM-2100F. XPS measurement was carried out by ESCALAB 250Xi (Thermo Fisher Scientific Inc.)

Perovskite solar cell fabrication

ITO-coated glasses were cleaned by sonication in detergent, followed by acetone, deionized water, and finally isopropyl alcohol. After 4 min of oxygen plasma treatment, a 30-nm-thick PEDOT:PSS was spin-coated on the ITO substrate and then annealed at 150 ℃ for 20 min using a hot plate. The perovskite precursor solution was then spin-coated on PEDOT:PSS at a speed of 3000 rpm for 40 s and

annealed at 100 ℃ for 45 min in an vacuum oven pumped down to ~ 1000 pa (Liu et al., 2018). A 40-nm-thick PCBM was spin-coated on the perovskite layer, followed by the deposition of Phen-NaDPO (3 nm) and Ag (100 nm) via thermal deposition in a high vacuum condition.

Perovskite solar cell characterization

The current density-voltage (J-V) characteristics of the devices were measured in a scan rate of 0.1 V/s and under 100 mW/cm^2 air mass 1.5 global (AM 1.5G) illumination with a solar simulator (Taiwan, Enlitech, SS-F5). The light intensity was calibrated using a National Renewable Energy Laboratory calibrated silicon photodiode with a KG5 filter. The device effective area was confirmed by a 0.04-cm^2 mask. The EQE study was performed on a commercial EQE measurement system (Taiwan, Enlitech, QE-R3011). The stability measurement under continuous illumination was measured by white-light LED sources with a total intensity of 100 mW/cm^2. For the transient photovoltage and transient photocurrent measurements, the device was serially connected to a digital oscilloscope (Tektronix TDS 3052C), and the oscilloscope's input impedance was set to 1 MΩ and 50 MΩ, respectively, to form the open- and short-circuit conditions. The transient photovoltage was measured under 0.3 Sun illumination. An attenuated laser pulse (0.54 μJ/cm^2; 530 nm) was used as a small perturbation to the device's background illumination. The device's transient photocurrent was measured by applying 530-nm laser pulses with a pulse width of 120 fs and a low pulse energy to the short-circuited devices in the dark. The laser pulses were generated from an optical parametric amplifier (TOPAS-Prime) pumped by a mode-locked Ti:sapphire oscillator seeded regenerative amplifier, with a pulse energy of 1.3 mJ at 800 nm and a repetition rate of 1 KHz (SpectraPhysics Spitfire Ace). The time resolution of the overall measurement is near 1 ns.

Supplemental Reference:

Liao Y., Liu H., Zhou W., Yang D., Shang Y., Shi Z., Li B., Jiang X., Zhang L., Quan L.N., et al., Highly oriented low-dimensional tin halide perovskites with enhanced stability and photovoltaic performance, *J. Am. Chem. Soc.* **139**, 2017, 6693–6699.

Zhao Z., Gu F., Li Y., Sun W., Ye S., Rao H., Liu Z., Bian Z. and Huang C., Mixed-organic-cation tin iodide for lead-free perovskite solar cells with an efficiency of 8.12%, *Adv. Sci. (Weinh)* **4**, 2017, 1700204.

Xu G., Bi P., Wang S., Xue R., Zhang J., Chen H., Chen W., Hao X., Li Y. and Li Y., Integrating ultrathin bulk-heterojunction organic semiconductor intermediary for high-performance low bandgap perovskite solar cells with low energy loss, *Adv. Funct. Mater.* **28**, 2018, 1804427.

Wang Y., Fu W., Yan J., Chen J., Yang W. and Chen H., Low-bandgap mixed tin–lead iodide perovskite with large grains for high performance solar cells, *J. Mater. Chem. A* **6**, 2018, 13090–13095.

Yang Z., Rajagopal A. and Jen A.K.-Y., Ideal bandgap organic–inorganic hybrid perovskite solar cells, *Adv. Mater.* **29**, 2017, 1704418.

Yang Z., Rajagopal A., Chueh C.-C., Jo S.B., Liu B., Zhao T. and Jen A.K.-Y., Stable low-bandgap Pb–Sn binary perovskites for tandem solar cells, *Adv. Mater.* **28**, 2016, 8990–8997.

Zong Y., Zou Z., Chen M., Padture N.P. and Zhou Y., Lewis-adduct mediated grain-boundary functionalization for efficient ideal-bandgap perovskite solar cells with superior stability, *Adv. Energy Mater.* **8**, 2018, 1800997.

Xu X., Chueha C.-C., Yanga Z., Rajagopala A., Xua J., Joa S.B. and Jen A.K.-Y., Ascorbic acid as an effective antioxidant additive to enhance the efficiency and stability of Pb/Sn-based binary perovskite solar cells, *Nano Energy* **34**, 2017, 392–398.

Ke W., Stoumpos C.C., Zhu M., Mao L., Spanopoulos I., Liu J., Kontsevoi Q.Y., Chen M., Sarma D., Zhang Y., et al., Enhanced photovoltaic performance and stability with a new type of hollow 3D perovskite {en}FASnI$_3$, *Sci. Adv.* **3**, 2017, e1701293.

Liu C., Li W., Li H., Zhang C., Fan J. and Mai Y., C60 additive-assisted crystallization in CH$_3$NH$_3$Pb$_{0.75}$Sn$_{0.25}$I$_3$ perovskite solar cells with high stability and efficiency, *Nanoscale* **9**, 2017, 13967–13975.

Liao W., Zhao D., Yu Y., Grice C.R., Wang C., Cimaroli A.J., Schulz P., Meng W., Zhu K., Xiong R.-G. and Yan Y., Lead-free inverted planar formamidinium tin triiodide perovskite solar cells achieving power conversion efficiencies up to 6.22%, *Adv. Mater.* **28**, 2016, 9333–9340.

Liu, M., Chen, Z., Xue, Q., Cheung, S. H., So, S.-K., Yip H.-L. and Cao Y. High performance low-bandgap perovskite solar cells based on high-quality mixed Sn-Pb perovskite film prepared by vacuum-assisted thermal annealing. *J. Mater. Chem. A* **6**, 2018, 16347-16354.